Stratospheric Ozone and the Morphology of the Northern Hemisphere Planetary Waveguide

John R. Albers[1], John P. McCormack[2], and Terrence R. Nathan[1]

[1] Department of Land, Air, and Water Resources: Atmospheric Science Program. University of California, Davis, CA, USA
[2] Space Science Division, Naval Research Laboratory, Washington D.C., USA

Abstract

A middle atmosphere general circulation model is used to examine the effects of zonally asymmetric ozone (ZAO) on the Northern Hemisphere planetary waveguide (PWG) during winter (December-February). The morphology of the PWG is measured by a refractive index, Eliassen-Palm flux vectors, the latitude of the subtropical zero wind line, and the latitude of the subtropical jet. ZAO causes the PWG to contract meridionally in the upper stratosphere, expand meridionally in the lower stratosphere, and expand vertically in the upper stratosphere and lower mesosphere. The ZAO-induced changes in the PWG are the result of increased upward and poleward flux of planetary wave activity into the extratropical stratosphere and lower mesosphere. These changes cause an increase in the Eliassen-Palm flux convergence at high latitudes, which produces a warmer and weaker stratospheric polar vortex and an increase in the frequency of stratospheric sudden warmings. The ability of ZAO to alter the flux of planetary wave activity into the polar vortex has important implications for accurately modeling wave-modulated and wave-driven phenomena in the middle atmosphere, including the 11-year solar cycle, stratospheric sudden warmings, and the phase of the Northern Hemisphere annular mode.

1. Introduction

The concept of a planetary waveguide (PWG) was first proposed by *Dickinson* [1968] to describe the regions of the Northern Hemisphere (NH) winter stratosphere where the background zonal wind supports the upward propagation of planetary waves. *Matsuno* [1970] expanded on *Dickinson's* PWG concept and derived a refractive index for planetary waves on a sphere and showed that planetary wave propagation is strongest in regions where the refractive index is large and positive. For a typical NH winter zonal wind distribution (Fig. 1), large, positive values of the refractive index occur in the region bounded on the south by the zero wind line [*Tung*, 1979] and on the north by the southern edge of the polar vortex [*Chapman and Miles*, 1981].

The zero wind line and the vortex edge do not, however, provide a complete description of planetary wave propagation within the PWG; indeed, there exist robust features of the background flow within the PWG that exert substantial control over how much planetary wave activity enters the PWG from the troposphere, and where that wave activity propagates once inside the stratosphere. For example, the vertical shear of the zonal-mean wind near the tropopause exerts significant influence over the amount of planetary wave activity that propagates upwards from the troposphere into the lower stratosphere [*Chen and Robinson*, 1992]. And once planetary waves arrive in the lower stratosphere, the local minimum in the refractive index associated with the negative vertical and horizontal gradients of the zonal-mean wind (above and to the north of the subtropical jet) splits the PWG into two 'channels' through which planetary wave activity may either propagate poleward and upward into the interior of the stratosphere, or equatorward where the waves are confined to the lower stratosphere [*Chapman and*

52 *Miles*, 1981; *Huang and Gambo*, 1982; *Li et al.*, 2006]. For the planetary waves that
53 propagate upward and poleward into the interior of the stratosphere, the height that
54 planetary waves are able to propagate is largely controlled by the ratio of the meridional
55 gradient of potential vorticity to the zonal-mean westerly wind [*Charney and Drazin*,
56 1961; *Matsuno*, 1970]. In addition, *Nigam and Lindzen* [1989] showed that modest
57 latitudinal shifts in the location of the subtropical jet greatly alter the amount of planetary
58 wave activity that is refracted into the mid-latitude and polar stratosphere. These results
59 show that the PWG is largely defined by its meridional width (measured by the location
60 of the zero wind line), its vertical extent (measured by the refractive index), and the
61 strength of wave propagation around the subtropical jet and within the waveguide (both
62 measured by the refractive index).

63 The structures of the zonal-mean wind and PWG are determined by a balance
64 between radiative heating due to ozone, longwave radiative cooling, and dynamical
65 heating due to planetary waves. Any physical process that alters this three-way balance
66 will in turn modulate the PWG. One such process involves the feedbacks between
67 planetary wave activity and stratospheric ozone. Specifically, as planetary waves
68 propagate from the troposphere into the stratosphere during NH winter, they produce
69 large zonal asymmetries (waves) in wind, temperature, and ozone [*Gabriel et al.*, 2007].
70 Observations show that zonally asymmetric ozone (ZAO) constitutes a significant
71 fraction of the total stratospheric ozone field (e.g., *Wang et al.*, 2005; *Gabriel et al.*,
72 2007; *Crook et al.*, 2008). That fraction reaches 10% during boreal winter (based on
73 decadal averages; *Crook et al.*, 2008); 15% in the lower stratosphere near ~70°N and
74 ~65°S [*Gillett et al.*, 2009]; 50% during the Antarctic stratospheric sudden warming of

2002 [*Wang et al.*, 2005]; and 50% during the breakup of the Antarctic ozone hole [*Crook et al.*, 2008]. The phasing between the wind, temperature, ozone waves produce fluxes that modulate both the spatial-temporal damping of the wave fields and the driving of the zonal-mean circulation [*Nathan and Li*, 1991; *Nathan and Cordero*, 2007; *Albers and Nathan*, 2012].

General circulation modeling studies have also shown that ZAO has a large effect on the zonal-mean temperature and wind structure of the wintertime middle atmosphere in both hemispheres [*Kirchner and Peters*, 2003; *Sassi et al.*, 2005; *Gabriel et al.*, 2007; *Brand et al., 2008; Crook et al.*, 2008; *Waugh et al.*, 2009; *Gillett et al.*, 2009; *McCormack et al.* 2011]. For example, *Crook et al.* [2008] examined the effect of ZAO on the high latitude Southern Hemisphere and found that including ZAO produces lower stratosphere cooling that is comparable in magnitude to the cooling produced by the springtime Antarctic ozone hole. In a study that focused on the Northern Hemisphere, *McCormack et al.* [2011] carried out an ensemble of GCM simulations over the December-March period and found that ZAO produces a warmer and more disturbed stratospheric polar vortex and an increased incidence of stratospheric sudden warmings (SSWs). Although *McCormack et al.* showed that ZAO changes temperatures and winds in the polar stratosphere, the mechanisms involved in the changes were not fully investigated; yet understanding the connections between ZAO and the polar stratosphere is vital to producing reliable assessments of human-caused impacts on key features of the climate system, including the upward flux of planetary wave activity, the frequency of SSWs, and the phase of the Northern Hemisphere annular mode. Here we investigate how the physics associated with ZAO changes the morphology of the PWG. The results

98 that we obtain underscore the importance of accurately accounting for ZAO in global
99 climate models.

100 In the following section we introduce the model and diagnostics that we use to
101 measure changes in the morphology of the PWG. In Section 3 we present our results, and
102 in Section 4 we discuss the implications of our results for global climate modeling.

103 2. Model Description and Diagnostics

104 We investigate the effects of ZAO on planetary wave propagation during NH
105 winter using the NOGAPS-ALPHA global spectral general circulation model [see, for
106 example, *Eckermann et al.,* 2009; *McCormack et al.,* 2011 and references therein].
107 NOGAPS-ALPHA extends from the surface to ~90 km in height and utilizes 68 hybrid
108 (σ-p) vertical levels with triangular truncation at wavenumber 79. The model includes
109 prognostic equations for O_3 and H_2O, which are calculated using the photochemical
110 parameterizations of *McCormack et al.* [2006, 2008]. Shortwave heating and longwave
111 cooling rates are computed using prognostic O_3 and H_2O fields and a fixed profile of
112 CO_2. Sea surface temperatures and ice distributions are specified at the model lower
113 boundary using 12-hourly observations from operational global analyses.

114 We analyze fifteen pairs of model simulations spanning early December to late
115 March (121 days). Each pair of simulations was initialized using identical profiles of
116 wind, temperature, and chemical constituents acquired from the NOGAPS-ALPHA data
117 assimilation system [*Eckermann et al.,* 2009]. The initialization dates were staggered in
118 time in order to generate an ensemble of fifteen independent pairs of model simulations
119 (for details see *McCormack et al.,* 2011). For each pair of simulations, one used fully
120 prognostic ozone in the radiative heating and cooling calculations (designated 3DO3),

and the other used zonal-mean values of the instantaneous prognostic ozone field to evaluate the radiative heating and cooling rates (designated ZMO3). We isolate the effect of ZAO on the circulation by taking the difference between 3DO3 and ZMO3 simulations for any given variable. When calculated in this way, the difference between the 3DO3 and ZMO3 simulations isolates the effect of ZAO-heating, but not the effect of changes in zonal-mean ozone heating due to wave-ozone transports. Consistent with *Albers and Nathan* [2012], however, the heating due to the wave-ozone transports is of secondary importance compared to the ZAO-heating. This means that the zonal-mean ozone distribution is similar for the 3DO3 and ZMO3 simulations.

Statistical significance of the differences between ensemble means of model variables is assessed using a Student's T-test at the 95% confidence level. As stated in *McCormack et al.* [2011], the 3DO3 model runs produced four SSWs, while the ZMO3 runs produced only one SSW. Statistical significance calculations were also carried out with all of the runs containing SSWs removed. Doing so did not change the qualitative nature of our results.

We evaluate the morphology of the PWG in terms of two properties: (i) its shape, measured by its vertical extent and meridional width; and (ii) by the strength and direction of wave propagation within the waveguide itself. To measure these properties we use a refractive index, Eliassen-Palm flux vectors, the latitude of the subtropical zero wind line, and the latitude of the subtropical jet.

To diagnose the shape of the PWG and to distinguish regions of wave propagation versus evanescence, we employ the spherical form of the quasigeostrophic refractive index squared [*Andrews et al.*, 1987]:

$$n_s^2(\phi, z) = \frac{\bar{q}_\phi}{\bar{u}} - \left(\frac{s}{a\cos\phi} \right)^2 - \left(\frac{f}{2NH} \right)^2, \quad (1)$$

where

$$\bar{q}_\phi = \frac{2\Omega\cos\phi}{a} - \frac{1}{a^2}\left(\frac{(\cos\phi\, \bar{u}_\phi)_\phi}{\cos\phi} \right)_\phi - \frac{f^2}{\rho}\left(\rho\, \frac{\bar{u}_z}{N^2} \right)_z \quad (2)$$

is the zonal-mean potential vorticity gradient; $\bar{u}$ is the zonal mean wind; ϕ is latitude, *z* is height, *s* is the spherical integer zonal wavenumber, *N(z)* is the buoyancy frequency, *f* is the Coriolis parameter, *H* is the mean scale height [=7 km], ρ [$=\rho_0 \exp(-z/H)$] is the standard density in log-pressure coordinates, ρ_0 is the sea-level reference density, *a* is the radius of the Earth, Ω is the Earth's rotation frequency, and subscripts denote derivatives with respect to the given variable.

Planetary waves propagate in regions where $n_s^2 > 0$ and are evanescent in regions where $n_s^2 < 0$. Thus the vertical extent of the PWG is measured by the height where $n_s^2 = 0$. The meridional width of the PWG is determined by its northern and southern boundaries. We measure the northern boundary of the PWG by the latitude where n_s^2 becomes negative. The southern boundary of the PWG, however, cannot be measured directly by n_s^2. This is because $|n_s^2| \to \infty$ as $\bar{u} \to 0$, so that interpretation of n_s^2 near the subtropical zero wind line becomes problematic. What is important here is that near the zero wind line the sign of $\bar{u}$ largely controls the sign of n_s^2. We therefore use the location of the zero wind line as a measure of the southern boundary of the PWG, consistent with previous studies [e.g., *Holton and Tan*, 1982]. In addition, we also use the location of the subtropical jet as a diagnostic to measure wave propagation within the

PWG. This diagnostic is motivated by *Nigam and Lindzen* [1989] who showed that small shifts (<3° in latitude) in the location of the subtropical jet can greatly alter the guiding of planetary waves from the troposphere into the extratropical stratosphere.

When measuring changes in n_s^2, we examine the relative importance of the strength, shear, and curvature of the zonal-mean wind. Equation (1) shows that the strength of wave propagation within the PWG depends on the ratio of the potential vorticity gradient to the zonal-mean wind, where the potential vorticity gradient (2) depends on the shear and curvature of the wind. Equation (1) also shows that as the planetary wave wavenumber *s* increases, n_s^2 decreases; this explains why the propagation of planetary waves into the stratosphere is largely confined to planetary wave numbers *s*=1-3 [*Charney and Drazin*, 1961].

We measure the strength and direction of planetary wave propagation within the PWG by using two related diagnostics: the Eliassen-Palm flux (EP-flux) and n_s^2. For steady, slowly varying plane waves, the planetary wave group velocity is locally parallel to the EP-flux vector [*Edmon et al.*, 1980]. In addition, the EP-flux vector $\vec{F}$ is curved up the gradient of n_s, and in particular, is guided along ridges of n_s [*Palmer*, 1981; *Palmer, 1982; Karoly and Hoskins*, 1982]. The magnitude of the EP-flux vector $\vec{F}$ is related to n_s^2 by [*Palmer*, 1981; *Palmer*, 1982]:

$$\left\|\vec{F}\right\| = \frac{1}{2}\exp(-z/H)\psi_s^2 n_s/(af) \tag{3}$$

where $\vec{F}$ is defined in (4) and (5) below; ψ_s is the amplitude of a steady, conservative, linear wave with zonal wave number *s*. Regions of larger n_s^2 are associated with larger

EP-flux vectors and the trajectories of the EP-flux vectors are refracted up the gradient of n_s^2. Thus the EP-flux vector and n_s^2 provide a useful way of visualizing the propagation pattern of planetary waves in the latitude-height plane. Under quasigeostrophic conditions, the EP-flux vector [$\vec{F} = (F^{(\phi)}, F^{(z)})$] and its divergence are defined in log-pressure coordinates as [*Andrews et al.*, 1987]

$$F^{(\phi)} = -\rho a \cos\phi (\overline{u'v'}) \tag{4}$$

$$F^{(z)} = \rho a f \cos\phi (\overline{v'\theta'}) / \overline{\theta}_z \tag{5}$$

$$\nabla \cdot \vec{F} = \frac{1}{a\cos\phi} \frac{\partial}{\partial \phi} \left(F^{(\phi)} \cos\phi \right) + \frac{\partial}{\partial z} \left(F^{(z)} \right) \tag{6}$$

where u and v are the zonal and meridional winds and θ is the potential temperature; the overbars and primes denote zonal-mean and perturbation quantities, respectively; and the subscripts in (5) denote partial differentiation. In accordance with (4) and (5), an upward directed EP-flux vector corresponds to a poleward heat flux; an equatorward directed EP-flux vector corresponds to a poleward momentum flux. The divergence of the EP-flux (6) measures the net planetary wave driving of the zonal-mean wind. Specifically, negative values of the EP-flux divergence (i.e. convergence) exert a westward drag on the mean wind that weakens the winter stratospheric westerly winds. When plotting the EP-flux vectors and divergence, we adopt the scaling procedure of *Butchart et al.* [1982], which ensures that the relative size of the EP-flux vector components are preserved when plotted in Cartesian coordinates. For this scaling, the vector components (4) and (5) are multiplied by $2\pi a \cos\phi$ and (4) is additionally multiplied by c=0.0091; the units of the rescaled EP-flux divergence are kg s^{-2}.

200 The relationship between n_s^2 and the direction and magnitude of the EP-flux has
201 been successfully used to describe a variety of stratospheric phenomenon including
202 stratospheric sudden warmings [*Butchart et al.*, 1982; *Palmer*, 1981], decadal
203 temperature and circulation trends [*Hu et al.*, 2005], annular mode variability [*Lorenz*
204 *and Hartmann*, 2002], and the propagation of planetary waves between the troposphere
205 and stratosphere [*Chen and Robinson*, 1992]. However, n_s^2 and its connection to the EP-
206 flux are built on several simplifying assumptions that may not be valid under some
207 circumstances.

208 For example, *Harnik and Lindzen* [2001] have shown that when the middle
209 stratosphere contains a reflecting surface, the traditional n_s^2 (1) may be an unreliable
210 measure of the boundaries of the PWG. This is because n_s^2 (1) is a bulk quantity that does
211 not distinguish between propagation in the meridional and vertical directions. In fact,
212 vertical propagation may be squelched while n_s^2 remains positive. This can occur when
213 meridional propagation is sufficiently strong. This point was underscored by *Harnik and*
214 *Lindzen* who defined a wavenumber diagnostic, which, together with a linear model,
215 provided boundaries for meridional and vertical wave propagation. Using the diagnostic
216 for specific cases during Southern Hemisphere winter, they found that when a reflecting
217 surface formed in the upper stratosphere, it was about 10 km lower than that produced by
218 the traditional n_s^2.

219 Because the differences between the *Harnik and Lindzen* [2001] wavenumber
220 diagnostic and the traditional n_s^2 diagnostic appear to be largest when reflecting surfaces
221 form in the upper stratosphere, we calculated a reflection index following *Perlwitz and*

Harnik [2003] for all of our 3DO3 and ZMO3 model simulations. We found that for the 3DO3 ensemble simulations, 6 out of 15 Januarys had reflective surfaces in the upper stratosphere. For the ZMO3 simulations, only 3 out of 15 winters had reflective surfaces (one in December and two in January). For the February simulations there were no reflective surfaces in the upper stratosphere. For this reason, and since February is also the time when our simulations show that ZAO has its strongest effect on the model circulation (see Section 3), we can expect n_s^2 to be a representative measure of the morphology of the planetary wave guide.

Another potential concern regarding the diagnosis of wave propagation using (1)-(6) is that the mathematical relationship between the EP-flux and n_s^2 formally holds for slowly varying plane waves and for sufficiently small wave damping. These conditions may not be met in the real atmosphere due to wave reflection, tunneling, or damping, which may complicate the interpretation of the n_s^2/EP-flux relationship or invalidate it altogether [*Harnik* 2002].

The above caveats notwithstanding, our results will show that the relationship between the EP-flux divergence and n_s^2 explains a significant portion of the wind and PWG variability observed in the model simulations that include ZAO.

3. Results

We compare the morphology of the PWG for the ZMO3 and 3DO3 cases for the winter months of December, January, and February (DJF). We follow with a discussion describing how ZAO causes the morphology of the PWG to evolve differently during January and February.

3.1. Mean Winter Results (December-January-February)

Figures 1 and 2 show, respectively, the ZMO3 and 3DO3 ensemble mean zonal-mean wind and n_s^2 for stationary planetary wave s=1 averaged over DJF; similar results were obtained for planetary wave s=2 (not shown). Figures 1 and 2 show features of n_s^2 that are common to previous studies of NH planetary wave propagation (*Chapman and Miles*, 1981; *Chen and Robinson*, 1992). These features include a local minimum in n_s^2 in the middle latitude lower stratosphere (~42°N latitude at 20 km) and a local maximum in n_s^2 between 50°-60°N latitude and 25-30 km. The local minimum in n_s^2 is due to the large negative gradient in potential vorticity (2). The large potential vorticity gradient results from the negative vertical and meridional gradients in zonal-mean wind located just above and to the north of the subtropical jet (Figure 1a). For waves originating in the extratropical troposphere, the local minimum in n_s^2 in the lower stratosphere splits the vertical propagation of planetary waves along two 'channels' [*Chapman and Miles*, 1981; *Huang and Gambo*, 1982; *Li et al.*, 2006]. The splitting of wave propagation along two wave channels is a common feature of the NH PWG during the mid- to late winter (the time period of interest in this study), but may be less common during the early winter months of November-December (compare Figure 9 bottom left and bottom right of *Shaw et al.*, 2010). We shall refer to the two channels as the southern and northern wave channels.

Along the southern channel of the PWG, the planetary waves are confined to the lower to middle stratosphere where they are refracted equatorward, eventually dissipating before they reach the upper stratosphere. Along the northern channel, the waves propagate through the local maximum in n_s^2 associated with the weak westerly winds

267 located slightly north of the region between the subtropical and polar night jets. The
268 region between the jets is centered at ~56°N latitude and 25 km in Figure 1a. From the
269 local maximum in n_s^2, waves tend to propagate upwards along the southern edge of the
270 vertical axis of the polar night jet, where wave propagation is enhanced due to the
271 combination of positive vertical and meridional shear of the zonal-mean wind. Waves
272 that emanate from the sub-polar and polar regions tend to merge into the guide formed by
273 the northern channel. The EP-flux vectors shown in Figures 1b and 2b clearly show
274 planetary wave propagation along these two channels.

275 Planetary wave activity within the PWG is generally strongest during mid- to late
276 winter, when the polar vortex is generally weaker. This is consistent with *Charney and*
277 *Drazin* [1961] who showed that planetary wave propagation from the troposphere into the
278 stratosphere is favored in westerly flows that are not too strong. Because NH zonal
279 asymmetries in ozone are predominantly generated by planetary wave activity, we also
280 expect the ZAO field to be largest in late winter [*Peters and Entzian*, 1999; *Peters et al.*,
281 2008]. As winter wanes, the solar zenith angle decreases and the ozone heating becomes
282 stronger. Thus we can anticipate that the effects of ZAO, particularly with regard to the
283 PWG, will be strongest in mid- to late winter. This is indeed the case, and in the
284 discussion that follows, we focus our attention on January and February.

285 *McCormack et al.* [2011], in a preliminary study examining the effects of ZAO on
286 the NH wintertime circulation, found that ZAO has the largest affect on the dynamics of
287 the NH polar winter stratosphere during January and February. Figures 3a and 3b show
288 the difference in the ensemble mean zonal-mean wind (3DO3 minus ZMO3) for January
289 and February. Wind differences that are statistically significant above the 95%

confidence level are shaded. Overall, the effects of ZAO produce weaker westerly flow. During January (Fig. 3a), the largest ensemble mean differences (~10 m/s) are located throughout the tropical stratopause region. During February (Fig. 3b), the zonal wind differences extend poleward and downward with the largest differences (~17 m/s) located in the polar region between 40-50 km. Although the largest change in the wind speed occurs in February in the NH, changes in n_s^2 and the EP-flux divergence begin in January and grow as the winter season proceeds. By February there is a large change in wind speed in the extratropical stratosphere. We next consider January and February in more detail.

3.2. January Results

Figures 4a and 4b show the 3DO3 EP-flux divergence and EP-flux difference (3DO3 minus ZMO3) contours for January. Also shown are the corresponding EP-flux vectors. Figure 4b shows two important changes in the EP-flux due to ZAO. First, between 10-15 km and ~10°-50°N latitude, the EP-flux difference vectors are directed poleward. This corresponds to an increase in equatorward momentum flux, which is associated with the weakened extratropical upper tropospheric and lower stratospheric westerly flow. Second, between 10-30 km and ~50°-80°N latitude, the EP-flux difference vectors are directed upwards. This represents an increase in both vertical wave propagation and the meridional heat flux, which is associated with the weakening of the westerly flow. The change in the momentum flux in January continues to grow as the winter proceeds and will be important for explaining the equatorward shift in the subtropical jet seen later in February (Figure 3b). The effect of the increased meridional heat flux on the PWG, however, becomes readily apparent by the end of January.

313 ZAO affects the zonal-mean wind, and by extension n_s^2, via two pathways [*Albers*
314 *and Nathan*, 2012]. Along the first pathway, ozone-flux convergences due to ZAO
315 modify the zonal-mean ozone field. The change to the zonal-mean ozone field produces
316 changes in the zonal-mean radiative heating rate and thus the zonal-mean temperature. To
317 maintain thermal wind balance, the changes to the zonal-mean temperature result in
318 changes to the zonal-mean wind. Along the second pathway, ZAO-heating affects the EP-
319 flux divergence, which in turn also modulates the zonal-mean wind. However, the
320 difference between the 3DO3 and ZMO3 zonal-mean ozone fields is small between
321 December and mid-February, which means that the first pathway plays a minor role in
322 driving the changes to n_s^2 in the 3DO3 simulations. As a result, any changes in the zonal-
323 mean wind and n_s^2 during this time period must be due to changes in the EP-flux
324 divergence associated with ZAO-heating.

325 Figure 4b shows that the increase in the EP-flux divergence within the northern
326 channel of the PWG is primarily due to an increase in the vertical component of the EP-
327 flux vector (this is confirmed by the near verticality of the EP-flux difference vectors in
328 this region). To confirm that changes in the meridional heat flux precede changes in n_s^2
329 within the northern channel of the PWG, we next compare the time evolution of the
330 meridional heat flux and n_s^2.

331 Figure 5 shows the time series of the ensemble mean and area weighted average
332 of the meridional heat flux and n_s^2. The time series spans December 1 to February 28 and
333 the area weighted average is between 50°-75°N at ~27 km in height. This height and
334 latitude band lies roughly in the center of the northern channel of the PWG. During the

time period considered, the heat flux and n_s^2 exhibit qualitatively different behaviors before and after January 5.

Prior to January 5, the difference between the 3DO3 and ZMO3 heat fluxes (Figure 5a) does not produce a significance difference in the respective values of n_s^2 (Figure 5b). In contrast, after January 5, the heat flux of 3DO3 remains larger than the heat flux of ZMO3 (the exception is a small two-day period just after Jan. 10). As a result, n_s^2 for the 3DO3 ensembles also become larger than n_s^2 for the ZMO3 ensembles during mid- to late-January. Yet there are two important differences between the temporal evolution of the n_s^2 versus the heat flux. First, the increase in the 3DO3 n_s^2 lags the increase in the 3DO3 heat flux by ~5 days. Second, the increase in the 3DO3 n_s^2 remains rather small until the final 5-10 days of January. The time lag between the change in the heat flux and the change in n_s^2 is not unexpected because it takes time for the ZAO-induced changes in the planetary waves to be manifest as changes in the zonal-mean wind. Once the ZAO-heating triggers the initial increase in the meridional heat flux, however, a positive feedback cycle is initiated that ultimately affects the PWG and any subsequent planetary wave activity. In short, the initial increase in the EP-flux convergence due to ZAO-heating causes changes in the strength of the extratropical westerly flow and the meridional potential vorticity gradient that combine to increase n_s^2. The increase in n_s^2, in turn, causes a further increase in vertical wave propagation that reinforces the initial increase in the EP-flux convergence. To gain further insight into the increase in vertical wave propagation, we next consider the spatial evolution of the vertical component of the EP-flux ($F^{(z)}$) and the PWG.

Figure 6a shows contours of the January ensemble mean difference (3DO3 minus ZMO3) in $F^{(z)}$ (5). The increase in $F^{(z)}$ is primarily concentrated in two plumes located within the northern and southern wave channels. The primary plume originates in the sub-polar and polar latitudes centered at ~60°N latitude, while the second, smaller plume is centered at ~30°N latitude. The two plumes and the gap between them are representative of three features of the PWG discussed in Section 3.1; that is, the plumes represent an increase in vertical wave propagation along both the northern and southern planetary wave channels, while the gap between the plumes of $F^{(z)}$ is likely due to the local minimum in n_s^2 seen in Figures 1b and 2b at ~42°N latitude and 20 km.

To examine the connection between the increase in $F^{(z)}$ along each of the planetary wave channels and changes in the morphology of the PWG, we computed the change in n_s^2 (3DO3 minus ZMO3) for two periods during January. Guided by the n_s^2 time series in Figure 5, we calculated the change in n_s^2 between January 1-25 and January 25-31. Between January 1-25, there is very little change in n_s^2 (not shown); this result is consistent with the relatively small change in the January monthly mean zonal-mean wind shown in Figure 3a and the n_s^2 time series shown in Figure 5b. The final 5 days of January, however, show changes in n_s^2 that match very well with the increase in vertical wave propagation. In particular, the two plumes in $F^{(z)}$ shown in Figure 6a are collocated with notable increases in n_s^2 along both planetary wave channels (Figure 6b).

We next examine how the ZAO-related changes in the PWG that first appear in late January expand and amplify to produce the large change in the zonal wind in February.

379 **3.3. February Results**

380 Figure 3b shows that ZAO produces statistically significant decreases in the
381 zonal-mean westerly flow of 5-11 ms^{-1} in the equatorial upper stratosphere and middle
382 mesosphere, as well as decreases of 3-18 ms^{-1} throughout the NH extratropical
383 stratosphere and mesosphere during February. A third, smaller region of statistically
384 significant wind difference is located near the location of the subtropical jet at ~30°N in
385 the upper troposphere and lower stratosphere (UTLS); the wind change at this location
386 represents an increase of ~1-3 ms^{-1}. The differences in the NH zonal-mean wind show
387 three notable results. First, the decrease in the wind speed in the tropical upper
388 stratosphere and lower mesosphere causes a northward migration of the tropical easterlies
389 and a northward shift of the zero wind line. As Figure 7 shows, the northward shift in the
390 zero wind line varies from about 1° to 8° latitude between about 30 km and 65 km in
391 height. Second, the decrease in wind speed within the extratropics and polar region
392 represents a weaker polar vortex and a warmer stratosphere (see also *McCormack et al.*
393 [2011], their Figure 2). Third, the increased wind speed in the subtropical UTLS shifts
394 the subtropical jet equatorward by about 3°. The zonal wind differences in Figure 3 and
395 Figure 7 qualitatively agree with recent studies suggesting a connection between
396 northward shifts in the upper stratospheric zero wind line and an increase in the
397 frequency of SSWs. For example, *Gray* [2003] found that similar to the so-called
398 'Holton-Tan' mechanism in the lower stratosphere [*Holton and Tan,* 1982], a northward
399 shift in the upper stratospheric zero wind line produces a narrower PWG that directs more
400 planetary wave activity poleward. The increase in planetary wave activity induces more
401 wave drag on the zonal-mean circulation and creates a warmer extratropical and polar

stratosphere and an increased incidence of SSWs. Indeed, as our EP-flux diagnostics will show, the combination of a narrower PWG and an increase in wave propagation combine to produce an increase in wave drag, the weaker polar vortex shown in Figures 1a and 2a, and an increased incidence of major SSWs (four in the 3DO3 ensembles versus one in the ZMO3 ensembles).

Figures 8a and 8b compare values of the February ensemble mean n_s^2 (1) for ZMO3 and 3DO3 for stationary planetary wave s=1. The n_s^2 scale varies from red to blue, which corresponds with large to small n_s^2, respectively. Regions where planetary waves are evanescent (n_s^2<0) are denoted by white space. In addition to showing n_s^2, Figures 8a and 8b are overlaid with a qualitative outline of the PWG where values at either extreme of the n_s^2 scale are excluded and shaded by the transparent light grey color; the solid black line that outlines the PWG traces the 15 and 65 n_s^2 contours on the poleward and equatorward side of the PWG, respectively. Outlining the PWG this way greatly aids in visualizing changes to n_s^2; moreover, excluding the extreme values of n_s^2 is a physically reasonable approximation for two reasons. First, approaching the subtropical zero wind line, $n_s^2 \to \infty$ as $\bar{u} \to 0$. In this limit, n_s^2 becomes an unreliable measure of wave propagation. Second, because planetary waves tend to propagate towards and through large values of n_s^2, changes in n_s^2 within the region of very small n_s^2 on the poleward side of the PWG play a minor role in determining where planetary waves propagate. Regardless, choosing different extreme values to exclude from the PWG outline does not change the qualitative nature of our results.

423 Figure 8 shows that ZAO increases planetary wave propagation in three important
424 ways. First, the vertical extent of the PWG increases, which allows the waves to
425 propagate 10 to 15 km higher within the mesosphere between 45°-70°N. Second, ZAO
426 causes an increase in the magnitude of n_s^2 throughout the entire stratosphere, and in
427 particular, an increase in wave propagation along both the southern and northern wave
428 channels. The increase in n_s^2 along the southern wave channel is significant beginning at
429 the surface and extending upwards to ~35 km between 30°-40°N. The increase in n_s^2
430 within the northern wave channel extends upwards from ~20 km all the way to into the
431 mesosphere near ~75 km. And third, ZAO also causes a significant increase in n_s^2 in the
432 polar UTLS between ~60°-80°N. The increases in wave propagation described above are
433 each due to different structural changes in the wind and are embodied by competing
434 terms in n_s^2 (1), namely, the strength of the zonal mean wind versus the meridional
435 potential vorticity gradient.

436 According to the first term on the RHS of (1), weaker westerly winds and
437 increases in the meridional potential vorticity gradient together increase n_s^2. Ozone-
438 induced changes in the potential vorticity gradient, in turn, are due to changes in the
439 meridional and vertical shear terms of the zonal-mean wind [the second and third terms
440 on the RHS of (2)]. We compared each of the terms in (2) for the 3DO3 and ZMO3 sets
441 of ensembles and found that nearly all of the changes in n_s^2 due to changes in the
442 potential vorticity gradient are due to the third term on the RHS of (2). Further details can
443 then be exposed by expanding the third term on the RHS of (2), which yields

$$-\frac{f^2}{\rho_s}\left(\rho_s \frac{\bar{u}_z}{N^2}\right)_z = \left(\frac{f^2}{HN^2} + \frac{f^2}{N^4}\frac{dN^2}{dz}\right)\bar{u}_z - \frac{f^2}{N^2}\bar{u}_{zz}\,. \tag{7}$$

The first term on the RHS of (7) is proportional to the vertical shear of the mean wind, while the second term is proportional to the vertical curvature of the mean wind. Thus an increase in positive vertical wind shear (or a decrease in negative vertical wind shear) increases the meridional potential vorticity gradient (2) and increases n_s^2 (1). Based on a numerical comparison of the two terms on the RHS of (7), we found that the vertical shear term is the dominant term and largely accounts for changes between the 3DO3 and ZMO3 ensembles. Thus the changes in n_s^2 shown in Figure 8 can be explained by the ratio $\bar{u}_z / \bar{u}$.

With the exception of the UTLS region along the southern wave channel, the entire extratropical stratosphere and lower mesosphere is characterized by weakened westerly winds (Figure 3b), consistent with an increase in n_s^2 within the PWG shown in Figure 8. The weakened polar vortex in the 3DO3 simulations, however, also affects the vertical wind shear. Figure 2a shows that the location of the maximum wind speed in the vortex core extends from ~60 km at ~40°N to ~40 km at ~60°N, so that much of the region above ~40-50 km is characterized by negative vertical wind shear, while the region below ~40 km is largely characterized by positive vertical wind shear. These features are clearly seen in Figure 9a, which depicts the change in the vertical wind shear between the 3DO3 and ZMO3 ensembles. As a consequence of the weaker polar vortex in the 3DO3 simulations, the vertical wind shear along the upper portion of the northern wave channel (between 40°-70°N and above ~40 km) and along the southern wave channel (between 30°-40°N in the UTLS) becomes weaker (less negative); this

contributes positively to the increase in n_s^2. In contrast, the region along the lower portion of the northern wave channel (between ~55°-85°N and 10-40 km) is characterized by a decrease in positive vertical wind shear that contributes negatively to n_s^2; thus the increase in n_s^2 in the this region is due solely to the weakened westerly winds in the 3DO3 simulations. Each of the changes in the magnitude and vertical shear of the zonal-mean wind just described will prove to be important for explaining the increases in the February EP-flux convergence as discussed in the next section.

3.4. Discussion

We have shown that ZAO-heating causes an increase in the EP-flux beginning in early to mid-January. This initial increase in the EP-flux produces changes in the zonal-mean wind that are manifest as changes in the PWG. The changes in the PWG occur via variations in the location of the subtropical jet, shifts in the latitude of the subtropical zero wind line, and the strength of wave propagation within the extratropical stratosphere. These changes in the EP-flux and PWG represent a positive feedback, where the initial ZAO-induced changes in wave amplification/damping trigger changes in the PWG that affect subsequent planetary wave activity entering the stratosphere. As the winter season progresses the ZAO-induced changes in the PWG become increasingly important.

To better understand how ZAO affects the PWG during late January and February, we consider how the ZAO-weakened lower stratospheric zonal winds combine with the equatorward shift in the subtropical jet. First some background.

Using a primitive equation model, *Nigam and Lindzen* [1989] found that small perturbations (< 5 ms^{-1}) to the zonal-mean wind could produce equatorward shifts in the location of the subtropical jet. Although small, these shifts could nonetheless

488 substantially enhance the guiding of planetary waves from their primary source region
489 (the Himalayas at ~27°N) into the polar stratosphere. Similarly, *Hu and Tung* [2002]
490 showed that the low index phase of the Northern Hemispheric annular mode (which is
491 characterized by an equatorward shift in the NH zonal jet), is associated with weakened
492 zonal-mean winds and increased n_s^2 in the UTLS region between 60°-80°N. In addition
493 to changes in n_s^2, *Limpasuvan and Hartmann* [2000] showed that the low index phase of
494 the Northern annular mode is also characterized by anomalous increases in poleward
495 directed EP-flux vectors; the resulting increase in equatorward momentum fluxes are
496 associated with a weakened stratospheric westerly winds. Our results suggest that ZAO
497 modulates n_s^2 and the EP-flux in a similar fashion to each of the phenomenon described
498 by *Nigam and Lindzen*, *Hu and Tung*, and *Limpasuvan and Hartmann*. Indeed, the
499 equatorward shift in the subtropical jet in the 3DO3 simulations is accompanied by: an
500 anomalous increase in upward directed EP-flux vectors into the stratosphere and an
501 anomalous increase in poleward directed EP-flux vectors in the UTLS between ~30°-
502 75°N (Figure 9b); weakened westerly winds (Figure 3b); and increased n_s^2 values (Figure
503 8b) throughout the extratropical UTLS. The increase in the anomalous poleward and
504 upward directed EP-flux vectors observed in February reinforce the positive feedback
505 cycle between the EP-flux convergence and n_s^2 first established in late January; the net
506 result is an increase in wave propagation throughout both channels of the PWG. To better
507 understand the implications of the expansion of the PWG in the vertical and the increase
508 in wave propagation within the PWG, we next consider the EP-flux convergence.

509 Figures 10a shows contours of the difference (3DO3 minus ZMO3) of the EP-flux
510 convergence in February. In a continuation of the EP-flux convergence differences that

511 first appeared in January, the February difference clearly shows two plumes of increased
512 convergence along both the northern and southern wave channels. There is a 30-50%
513 increase in the EP-flux convergence along the northern wave channel between 15-20 km,
514 and a 15-100% increase along the southern wave channel at the same heights. As in
515 January, the two plumes of increased EP-flux convergence correspond with significant
516 increases in vertical wave propagation; this can be verified by examining the increased
517 EP-flux vectors in Figure 9b and more specifically, the increase in $F^{(z)}$ shown in Figure
518 10b. In addition to an increase in magnitude, the ZAO-induced increase in $F^{(z)}$ during
519 February also extends ~10-15 km higher than was observed during January (compare
520 Figures 6a and 10b); this is consistent with the 10-15 km increase in height of the
521 February PWG depicted in Figure 8.

522 The increases in vertical wave propagation along the northern and southern wave
523 channels, however, correspond to the qualitatively different changes in wind structure
524 described in Section 3.3. The increase in vertical wave propagation along the southern
525 wave channel (~30°-40°N) in the UTLS is due to a combination of changes in the vertical
526 shear, meridional shear, and curvature of the zonal-mean wind rather than changes in the
527 magnitude of the wind. This is verified in Figure 3b, which shows that the UTLS is
528 characterized by an increase in the mean wind that contributes negatively to the
529 magnitude of n_s^2. The dominant contribution to the increase in n_s^2 and the increased
530 vertical propagation along the southern wave channel is due to the increase in positive
531 vertical wind shear depicted in Figure 9a between ~30°-40°N. The meridional shear and
532 curvature terms (not shown) also contribute to the increase in n_s^2, but their contribution is
533 secondary to that of the vertical shear term. The importance of vertical wind shear along

534 the tropopause is perhaps not surprising in light of the study by *Chen and Robinson*
535 [1992] who showed that even small changes in vertical wind shear near the tropopause
536 may produce significant changes (20-40%) in n_s^2 and EP-flux convergence in the UTLS.
537 In contrast to the changes along the southern wave channel, the increase in vertical wave
538 propagation along the northern wave channel are due to increases in n_s^2 associated solely
539 with the weakened westerly winds; this is verified by noting the decrease in positive
540 vertical wind shear (Figure 9a) that contributes negatively to n_s^2.

541 Despite the similarities between the distributions in the January and February EP-
542 flux convergences (compare Figs. 4b and 10a), there are two notable changes between the
543 two months. First, the local minimum in the EP-flux convergence along the northern
544 wave channel (centered at ~60°N and 18 km) has increased slightly from -36 to -32 kg s^{-}
545 ^{2}, while the local minimum along the southern wave channel (centered at ~32°N and 16
546 km) has decreased by ~60% from -27 to -43 kg s^{-2}. This indicates that the local increase
547 in n_s^2 and the equatorward shift in the subtropical jet have combined to significantly
548 increase the poleward and vertical propagation of planetary waves (Figure 9b and 10b),
549 which results in the large increase in the EP-flux convergence along the southern wave
550 channel. Second, while the increased EP-flux convergence due to ZAO extended all the
551 way from the middle stratosphere down to the surface between 50°-70°N during January
552 (Figure 4b), there is no increase in convergence between ~10-15 km and 30°-70°N during
553 February (Figure 10a); this difference cannot be explained by the changes in n_s^2
554 described earlier. There are several possible explanations for this apparent discrepancy
555 between the increase in the EP-flux convergence and n_s^2.

556 One possible explanation for the increase in the EP-flux convergence in the UTLS
557 is associated with the ability of ZAO to alter the EP-flux convergence through wave
558 amplification/damping. Indeed it is ZAO-heating that triggers the initial increase in the
559 EP-flux convergence and the PWG in mid- to late-January described in Section 3.2. The
560 ozone-modified refractive index derived in *Nathan and Cordero* [2007] describes how
561 ZAO and zonal-mean ozone combine to alter both planetary wave propagation and wave
562 damping. *Albers and Nathan* [2012] subsequently used the ozone-modified refractive
563 index to show how changes in wave propagation and damping due to ZAO act together or
564 in opposition to produce small or large changes in the EP-flux in the lower stratosphere.
565 Although the current experimental setup does not make it possible to separate ZAO-
566 related effects due to wave propagation and wave damping, it is indeed possible that the
567 apparent discrepancy between the increase in n_s^2 seen in Figure 8 and decrease in the EP-
568 flux convergence seen between ~5-15 km and 30°-70°N in Figure 10 could be related to
569 ZAO-induced changes in wave damping and wave propagation that are not taken into
570 account by the inviscid form of n_s^2 (1) employed in this study. This issue will be the
571 subject of future modeling and observational studies.

572 A second possible explanation for the apparent discrepancy between the increase
573 in the EP-flux convergence and n_s^2 was discussed in Section 2. That is, wave tunneling or
574 wave reflection, separately or in combination, may invalidate the relationship between
575 the EP-flux and n_s^2 employed here [*Harnik* 2002]. In particular, whenever planetary
576 waves are propagating in the meridional plane they are likely undergoing horizontal
577 reflection because the wavelengths of the waves are longer than the width of the
578 waveguide (*Nili Harnik personal communication*). Thus because the EP-flux vectors

579 have a strong meridional component between ~10-15 km and 30°-50°N (Figures 1b and
580 2b), it is not surprising that the change in the propagation pattern of the EP-flux vectors is
581 not well described by the change in n_s^2 in this region. Yet a third possibility is that the
582 ZAO-induced changes in the stratospheric circulation have caused changes in the
583 troposphere that increase the generation of planetary wave activity. Indeed our results
584 show that ZAO affects the circulation of the troposphere (e.g., Figures 3 and 10a). Thus it
585 is possible that some of the increase in the EP-flux convergence in the UTLS is due to an
586 increase in planetary wave generation in the troposphere.

4. Summary and Conclusions

587 Using a middle atmosphere general circulation model, we have shown that
588 zonally asymmetric ozone (ZAO) alters the morphology of the PWG in three distinct
589 ways. First, the PWG contracts meridionally and expands vertically within the upper
590 stratosphere and lower mesosphere. Second, the magnitude of wave propagation
591 increases throughout the interior of the stratospheric waveguide between ~30°-75°N. And
592 third, the subtropical jet shifts equatorward. In combination, the changes in the shape and
593 strength of the PWG are associated with increased deceleration of the zonal-mean
594 westerly flow, resulting in a weaker and warmer stratospheric polar vortex. These
595 changes correlate well with the increased incidence of SSW's in the presence of ZAO
596 reported by *McCormack et al*. [2011].

597 Changes in the PWG have important implications for modeling SSWs, variations
598 in stratospheric dynamics associated with the 11-year solar cycle, and the Northern
599 Hemisphere annular mode (NAM). For example, *Charlton et al.* [2007] investigated the
600 ability of a series of GCMs – which did not consider the effects of ZAO on the PWG – to

601 generate an accurate number of SSWs. The results showed that most GCMs failed to
602 produce enough SSWs when compared to observations. In the current GCM study –
603 where we explicitly consider the effects of ZAO on the PWG – the model runs with ZAO
604 had a noticeably larger EP-flux emanating from the UTLS and produced a larger number
605 of SSWs compared to similar runs without ZAO. This increase in the EP-flux correlates
606 well with the increase in n_s^2 in the lower stratosphere, indicating that changes in the PWG
607 associated with ZAO may play an important role in modulating the flux of wave activity
608 entering the stratosphere from the troposphere, which is known to drive SSWs.

609 SSWs have also been correlated with a northward shift of tropical easterlies and
610 the zero wind line within the upper stratosphere and lower mesosphere [*Gray*, 2003;
611 *Vineeth et al.*, 2010]. *Gray et al.* [2003] hypothesized that because vertically propagating
612 planetary waves have vertical wavelengths comparable to the distance between the
613 tropopause and the upper stratosphere during mid- to late-winter, it is possible that shifts
614 of the zero wind line in the upper stratosphere help guide waves poleward in much the
615 same manner as the traditional Holton-Tan mechanism in the lower stratosphere.
616 Although our experiments were not designed to test *Gray et al.'s* hypothesis, it is
617 nonetheless interesting to note the correlation between the northward shift in the zero
618 wind line and the increase in frequency of SSWs in our model runs that include ZAO.

619 In addition to SSWs, two aspects of the PWG discussed in this study – the width
620 and strength – may provide a means for ZAO to communicate and amplify the 11-year
621 solar cycle signal. The relationship between the width of the PWG and solar-modulated
622 ZAO has been shown by *Cordero and Nathan* [2005] to be an important pathway for
623 communicating the solar signal to the quasi-biennial oscillation (see their Figure 1).

624 Because our results show that ZAO plays a role in modulating the upper stratospheric
625 tropical easterlies, it is therefore likely that in a similar manner to the *Cordero and*
626 *Nathan* solar- quasi-biennial oscillation mechanism, ZAO may also play a role in
627 modulating the semi-annual oscillation in the tropical upper stratosphere. Because the
628 semi-annual oscillation plays a dominant role in the location and timing of shifts in the
629 upper stratospheric zero wind line, modulation of the semi-annual oscillation by ZAO
630 may provide an important pathway for solar modulation of the width of the PWG. Indeed,
631 this is a topic that deserves further attention given the parallel timing of the peak in wind
632 modulation from ZAO in our results and the robust solar signal observed during mid- to
633 late-winter in the tropical upper stratosphere [e.g., *Labitzke and van Loon*, 1988; *Naito*
634 *and Hirota*, 1997]. In addition to solar modulation of the width of the waveguide, ZAO
635 also provides a way to change the strength of wave propagation within the waveguide
636 itself. This scenario is supported by work demonstrating the link between the 11-year
637 solar cycle and changes in wave propagation and planetary wave drag in the extratropical
638 stratosphere [*Nathan et al.*, 2011; *Gabriel et al.*, 2011].

639 Finally, we note that the analysis in this paper has examined the effects of ZAO
640 from a "bottom-up" perspective. From this perspective, ZAO enhances the amount of
641 planetary wave activity that is refracted into the interior of the stratosphere from the
642 troposphere below. This phenomenon can be understood as a positive feedback cycle
643 where increases in the EP-flux convergence cause wind changes that increase n_s^2 within
644 the PWG; the increase in n_s^2 within the PWG in turn leads to further increases in the
645 vertical propagation of planetary waves with subsequent increases in the EP-flux
646 convergence. However, changes in the upward flux of planetary wave activity and

consequent variations in local wave-mean flow interaction in the stratosphere can also drive downward propagating zonal-mean wind anomalies [*Plumb and Semeniuk*, 2003], a "top-down" effect. Such downward propagating wind anomalies have been shown to be important for stratosphere-troposphere communication [*Kodera and Kuroda*, 2000; *Christiansen*, 2001; *Polvani and Waugh*, 2004; *Perlwitz and Harnik*, 2004] and NAM variability [e.g. *Baldwin and Dunkerton*, 1999; *Limpasuvan and Hartmann*, 2000]. The model simulations examined in this paper provide evidence that *ZAO affects both the downward propagation of wind anomalies and the phase of the NAM*. The downward propagation of the wind anomalies is seen in the space-time evolution of the ZAO-induced wind anomalies depicted in Figure 3 and in *McCormack et al.* [2011] (see their Figures 4a-d). The effect of ZAO-heating on the phase of the NAM is seen in the equatorward shift in the subtropical jet and a weakened polar vortex (compare Figure 3 and Figure 7), which are both common features of the low index phase of the NAM. The equatorward shift in the subtropical jet shown in our results is consistent with the work of *Brand et al.* [2008] who found that including ZAO produces a shift in the NAM towards its low index phase; this indicates that the relationship between ZAO and shifts in the phase of the NAM is likely a robust result. We are currently investigating the effects of ZAO on downward signal propagation and annular mode variability.

Acknowledgments. We thank Dr. Nili Harnik and two anonymous reviewers for providing helpful comments on the manuscript. JRA and TRN were supported in part by NSF grant ATM-0733698 and by NASA/NRL grant NNH08AI67I. JPM was supported in part by the Office of Naval Research and in part by NASA Heliophysics Living with a Star TR&T Program award NNH08AI67I.

670

671 # References

672 Albers, J. R., and T. R. Nathan (2012), Pathways for communicating the effects of
673 stratospheric ozone to the polar vortex: Role of zonally asymmetric ozone, *J.*
674 *Atmos. Sci.*, 60, 785-801.

675 Andrews, D. G., J. R. Holton, and C. B. Leovy (1987), Middle Atmosphere Dynamics,
676 Elsevier, New York.

677 Baldwin, M. P., and T. J. Dunkerton (1999), Propagation of the Arctic Oscillation from the
678 stratosphere to the troposphere, *J. Geophys. Res.*, 104, 30937-30946.

679 Brand, S., K. Dethloff, D. Handorf (2008), Tropospheric circulation sensitivity to an
680 interactive stratospheric ozone, *Geophys. Res. Lett.*, *35*, L05809.

681 Butchart, N., S. A. Clough, T. N. Palmer, P. J. Trevelyan (1982), Simulations of an
682 observed stratospheric warming with quasigeostrophic refractive index as a model
683 diagnostic, *Q. J. R. Meteorol. Soc.*, *108*, 475-502.

684 Chapman, W. A., and T. Miles (1981), Planetary-scale wave guides in the troposphere
685 and stratosphere, *Nature*, 293, 108-112.

686 Charlton, A. J., et al. (2007), A new look at stratospheric sudden warmings. Part II:
687 Evaluation of numerical model simulations, *J. Clim.*, *20*, 470-488.

688 Charney, J. G., and P. G. Drazin (1961), Propagation of planetary-scale disturbances
689 from the lower to upper atmosphere, *J. Geophys. Res.*, 66, 83-109.

690 Chen, P., and W. A. Robinson (1992), Propagation of planetary waves between the
691 troposphere and stratosphere, *J. Atmos. Sci.*, 49, 2533-2545.

692 Christiansen, B. (2001), Downward propagation of zonal mean zonal wind anomalies
693 from the stratosphere to the troposphere: Model and reanalysis, *J. Geophys. Res.*,
694 **106,** 27 307–27 322.
695 Cordero, E. C., and T. R. Nathan (2005), A new pathway for communicating the 11-year
696 solar cycle signal to the QBO, *Geophys. Res. Lett.*, *32*, L18805.
697 Crook, J. A., N. P. Gillett, and S. P. Keeley (2008), Sensitivity of Southern Hemisphere
698 climate to zonal asymmetry in ozone, *Geophys. Res. Lett.*, *35*, L07806.
699 Dickinson, R. E. (1968), Planetary Rossby waves propagating vertically through weak
700 westerly wave guides, *J. Atmos. Sci. 25*, 984-1002.
701 Eckermann, S. D., et al. (2009). High-altitude data assimilation system experiments for
702 the Northern Hemisphere summer mesosphere season of 2007, *J. Atmos. Sol.*
703 *Terr. Phys.*, *71*, 531-551.
704 Edmon, H. J., B. J. Hoskins, M. E. McIntyre (1980), Eliassen-Palm cross sections for the
705 troposphere, *J. Atmos. Sci.*, *37*, 2600-2616.
706 Gabriel, A., D. Peters, I. Kirchner, and H. F. Graf. (2007), Effect of zonally asymmetric
707 ozone on stratospheric temperature and planetary wave propagation, *Geophys.*
708 *Res. Lett.*, *34*, L06807.
709 Gabriel, A., H. Schmidt, and D.H.W. Peters (2011), Effects of the 11-year solar cycle on
710 middle atmospheric stationary wave patterns in temperature, ozone, and water
711 vapor, *J. Geophys., Res*., 116, D23301.
712 Gillett, N. P., J. F. Scinocca, D. A. Plummer, M. C. Reader (2009), Sensitivity of climate
713 to dynamically-consistent zonal asymmetries in ozone, *Geophys. Res. Lett.*, *36*,
714 L10809.

715 Gray, L. J. (2003), The influence of the equatorial upper stratosphere on stratospheric
716 sudden warmings, *Geophys. Res. Lett., 30*, L041166.
717 Harnik, N., and R. S. Lindzen (2001), The effect of reflecting surfaces on vertical
718 structure and variability of stratospheric planetary waves, *J. Atmos. Sci.*, 58, 2872-
719 2894.
720 Harnik, N. (2002), The evolution of a stratospheric wave packet, *J. Atmos. Sci.*, 59, 202-
721 217.
722 Hu, Y., and K. K. Tung (2002), Interannual and decadal variations of planetary wave
723 activity, stratospheric cooling, and Northern Hemisphere annular mode, *J. Clim.*,
724 15, 1659-1673.
725 Hu, Y., K. K. Tung, and J. Liu (2005), A closer comparison of early and late-winter
726 atmospheric trends in the Northern Hemisphere, *J. Climate*, 18, 3204-3216.
727 Huang, R., and K. Gambo (1982), The response of a hemispheric multi-level model
728 atmosphere to forcing by topography and stationary heat sources (I) Forcing by
729 Topography, *J. Meteor. Soc. Japan*, 60, 78-92.
730 Holton, J. R., and H.C. Tan (1982), The quasi-biennial oscillation in the Northern
731 Hemisphere lower stratosphere, *J. Meteor. Soc. Japan*, *60*, 140-148.
732 Karloy, D. J., and B. J. Hoskins (1982), Three dimensional propagation of planetary waves,
733 *J. Meteor. Soc. Japan*, *60*, 109-123.
734 Kirchner, I., and D. Peters (2003), Modelling the wintertime response to upper tropospheric
735 and lower stratospheric ozone anomalies over the North Atlantic and Europe,
736 Annales Geophysicae, 21, 2107-2118.

737 Kodera, K., and Y. Kuroda (2000), A mechanistic model study of slowly propagating
738 coupled stratosphere–troposphere variability, *J. Geophys. Res.*, **105,** 12 361–12
739 370.
740 Labitzke, K., and H. van Loon (1988), Association between the 11-year solar cycle, the
741 QBO, and the atmosphere. Part I: The troposphere and stratosphere on the Northern
742 Hemisphere winter, *J. Atmos. Terr. Phys.*, *50*, 197-206.
743 Li, Q., H. F. Graf, and M. A. Giorgetta (2006), Stationary planetary wave propagation in
744 Northern Hemisphere winter – climatological analysis of the refractive index,
745 *Atmos. Chem. Phys. Discuss.*, 6, 9033-9067.
746 Limpasuvan, V., and D. L. Hartmann (2000), Wave-maintained annular modes of climate
747 variability, *J. Clim.*, 13, 4414-4429.
748 Lorenz, D. J., and D. L. Hartmann (2002), Eddy-zonal flow feedback in the Northern
749 Hemisphere winter, *J. Climate*, 16, 1212-1227.
750 Matsuno, T. (1970), Vertical propagation of stationary planetary waves in the winter
751 Northern Hemisphere, *J. Atmos. Sci. 27*, 871-883.
752 McCormack, J. P., S. D. Eckermann, D. E. Siskind, and T. J. McGee (2006), CHEM2D-
753 OPP: A new linearized gas-phase ozone photochemistry parameterization for high-
754 altitude NWP and climate models, *Atmos. Chem. Phys.*, *6*, 4943-4972.
755 McCormack, J. P., K. H. Hoppel, and D. S. Siskind (2008), Parameterization of middle
756 atmospheric water vapor photochemistry for high-altitude NWP and data
757 assimilation, *Atmos. Chem. Phys. Discuss.*, *8*, 13999-14032.
758 McCormack, J. P., T. R. Nathan, and E. C. Cordero (2011), The effect of zonally
759 asymmetric ozone heating on the Northern Hemisphere winter polar stratosphere,
760 *Geophys. Res. Lett.*, *38*, L03802.

761 Naito, Y., and I. Hirota (1997), Interannual variability of the northern winter stratospheric
762 circulation related to the QBO and the solar cycle, *J. Meteorol. Soc. Japan*, 75,
763 925-937.
764 Nathan, T. R., and L. Li (1991), Linear stability of free planetary waves in the presence
765 of radiative-photochemical feedbacks, *J. Atmos. Sci.*, 48, 1837-1855.
766 Nathan, T. R., and E. C. Cordero (2007), An ozone modified refractive index for
767 vertically propagating planetary waves, *J. Geophys. Res., 112*, D02105.
768 Nathan, T. R., J. R. Albers, and E. C. Cordero (2011), Role of wave-mean flow interaction
769 in sun-climate connections: Historical overview and some new interpretations and
770 results, *J. Atmos. Sol. Terr. Phys.*, 73, 1594-1605.
771 Nigam, S., and R. S. Lindzen (1989), The sensitivity of stationary waves to variations in
772 the basic state zonal flow, *J. Atmos. Sci.*, 46, 1746-1768.
773 Palmer, T. N. (1981), Aspects of stratospheric sudden warmings studied from a
774 transformed Eulerian-mean viewpoint, *J. Geophys. Res.*, 86, 9679-9687.
775 Palmer, T. N. (1982), Properties of the Eliassen-Palm flux for planetary scale motions, *J.*
776 *Atmos. Sci.*, 39, 992-997.
777 Peters, D., and G. Entzian (1999), Longitude-dependent decadal changes of total ozone in
778 boreal winter months during 1979-92, *J. Climate*, 12, 1038-1048.
779 Peters, D., A. Gabriel, and G. Entzian (2008), Longitude-dependent decadal ozone changes
780 and ozone trends in boreal winter months during 1960-2000, *Ann. Geophys.*, 26,
781 1275-1286.
782 Perlwitz, J., and N. Harnik (2003), Observational evidence of a stratospheric influence on
783 the troposphere by planetary wave reflection, *J. Climate*, 16, 3011-3026.

784 Perlwitz, J., and N. Harnik (2004), Downward coupling between the stratosphere and
785 troposphere: The relative roles of wave and zonal mean processes, *J. Climate*, 17,
786 4902-4909.
787 Plumb, R. A., and K. Semeniuk (2003), Downward migration of extratropical zonal wind
788 anomalies, *J. Geophys. Res*, 108, D74223.
789 Polvani, L. M. and D. W. Waugh (2004), Upward wave activity flux as a precursor to
790 extreme stratospheric events and subsequent anomalous surface weather regimes, *J.*
791 *Climate*, **17,** 3547–3553.
792 Sassi, F., B. A. Boville, D. Kinnison, R. R. Garcia (2005), The effects of interactive
793 ozone chemistry on simulations of the middle atmosphere, *Geophys. Res. Lett., 32*,
794 L07811.
795 Shaw, T. A., J. Perlwitz, and N. Harnik (2010), Downward wave coupling between the
796 stratosphere and troposphere: The importance of meridional wave guiding and
797 comparison with zonal-mean coupling, *23, J. Climate*, 6365-6381.
798 Tung, K. K. (1979), A theory of stationary long waves. Part III: Quasi-normal modes in a
799 singular waveguide, *J. Atmos. Sci. 107*, 751-774.
800 Vineeth, C., T. K. Pant, K. K. Kumar, S. G. Sumod (2010), Tropical connection to the
801 polar stratospheric sudden warming through quasi 16-day planetary wave, *Ann.*
802 *Geophys. 28*, 2007-2013.
803 Wang, et al. (2005), Longitudinal variations of temperature and ozone profiles observed by
804 MIPAS during the Antarctic stratosphere sudden warming of 2002, *J. Geophys.*
805 *Res., 110*, D20101.

806 Waugh, D. W., L. Oman, P. A. Newman, R. S. Stolarski, S. Pawson, J. E. Nielsen, and J.
807 Perlwitz (2009), Effects of zonal asymmetries in stratospheric ozone on simulated
808 Southern Hemisphere climate trends, *Geophys. Res. Lett*., *36*, L1870.
809

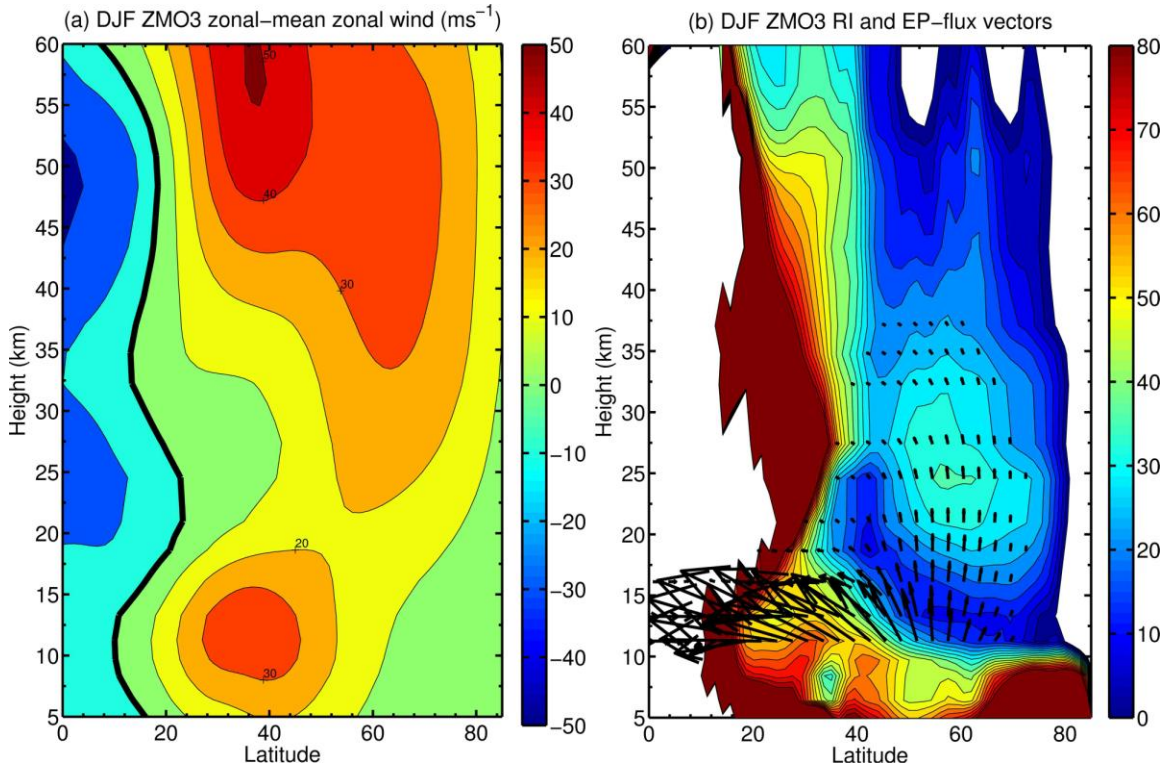

Figure 1. Three-month average (DJF) ZMO3 ensemble mean (a) zonal-mean wind and (b) n_s^2 with EP-flux vectors. In (a) the thick black line denotes the zero-wind line. In (b) the contours denote n_s^2, which has been non-dimensionalized with a^2 (contour interval is 4). The EP-flux vectors (arrows) are plotted only in regions where the EP-flux divergence is less than ~ -25x10^6 kg s^{-2} (this threshold eliminates visually distracting vectors that are inconsequential to the physics). The scaling of the EP-flux vectors is discussed in Section 2.

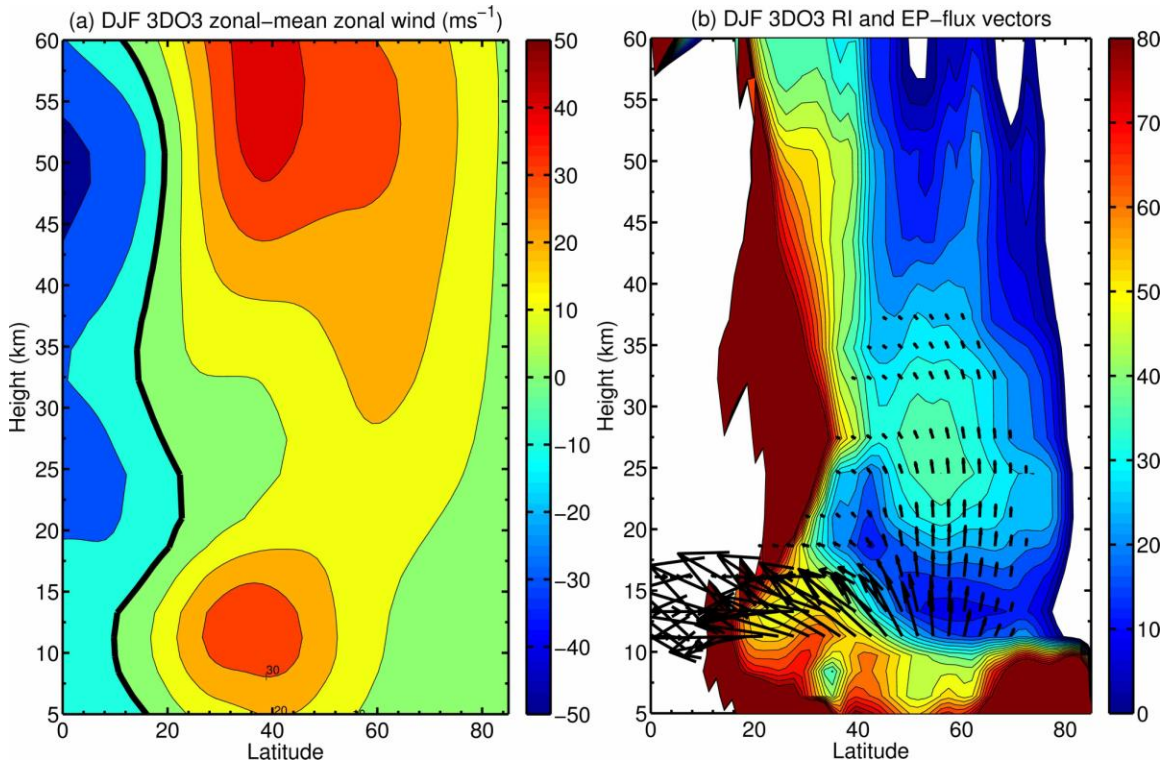

819

820 **Figure 2.** As in Figure 1, but for the 3DO3 ensemble mean.

821

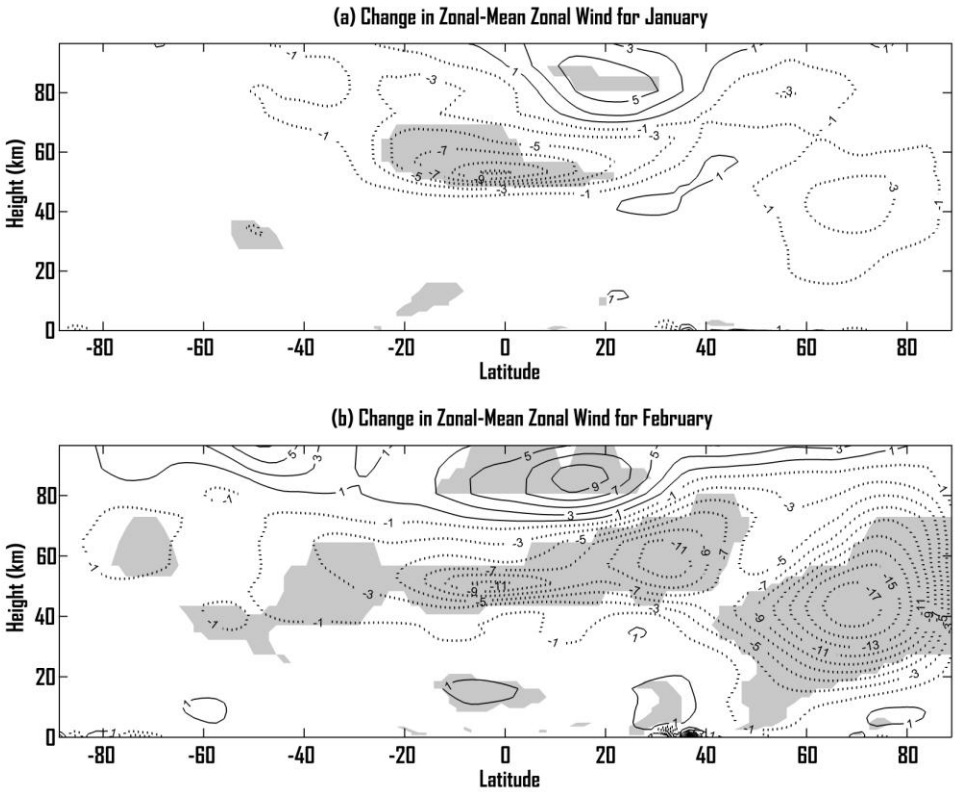

822

823 **Figure 3.** Monthly average zonal-mean wind difference (ΔU = 3DO3 minus ZMO3) for:
824 (a) January and (b) February. Contours intervals are in units of ms^{-1}. Statistically
825 significant wind changes at the 95% confidence level are shaded in gray.

826

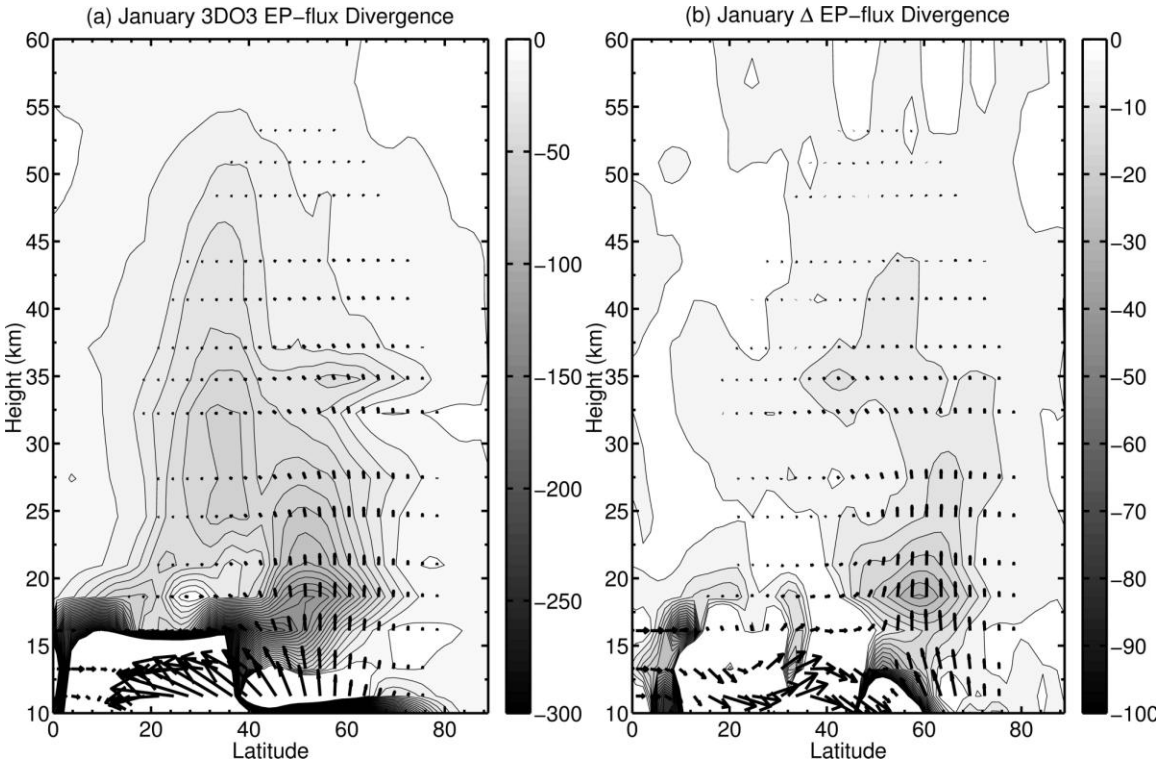

Figure 4. January ensemble mean for (a) 3DO3 EP-flux convergence with EP-flux vectors and (b) the difference (3DO3 minus ZMO3) in the EP-flux convergence and EP-flux vectors. In (a), the white region between 0°- 40°N latitude and below ~15 km represents EP-flux convergence that is greater than the 0 to -300 scale used for plotting. In both plots the units are $1x10^6$ kg s^{-2} and the contour interval is $5x10^6$ kg s^{-2}. As in Figures 1 and 2, the EP-flux vectors in (b) are only plotted in regions where the EP-flux divergence is less than the threshold ~ $-25x10^6$ kg s^{-2}. The scaling of the EP-flux vectors is discussed in Section 2; the magnitude of the vectors in (a) and (b) are consistent with the EP-flux convergence scale shown alongside each plot.

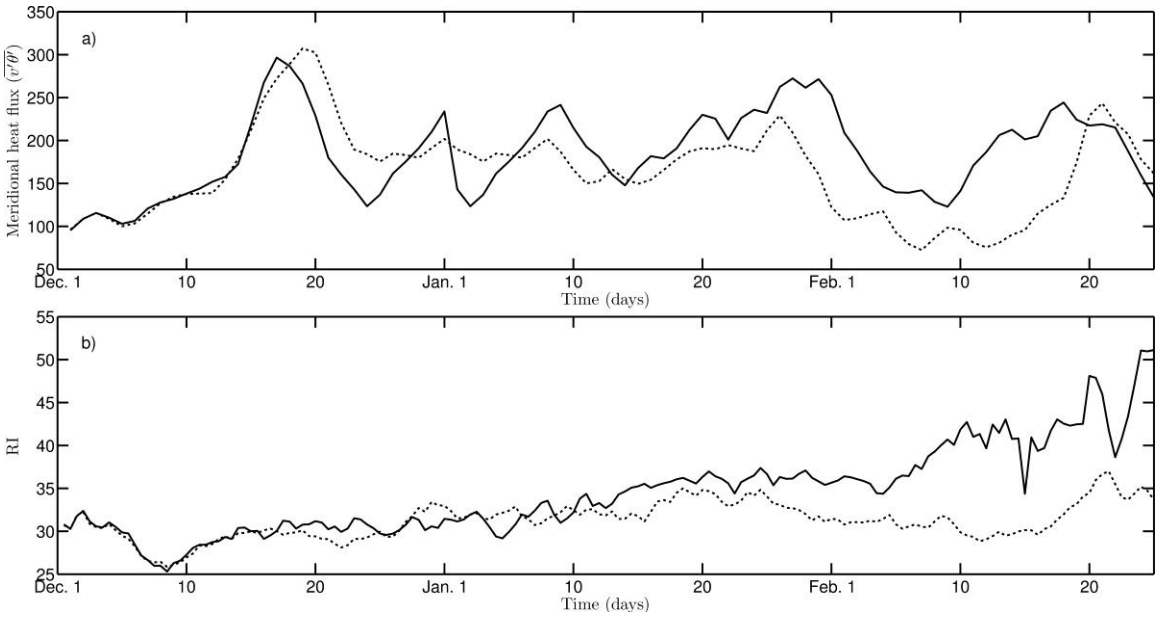

838

839 **Figure 5.** Time series of ensemble mean, area-weighted average (50°-75°N) at ~27 km for
840 the (a) meridional heat flux and (b) n_s^2 between December-February for 3DO3 (solid lines)
841 and ZMO3 (dotted lines). The heat flux is in units of K ms^{-1}, while n_s^2 has been non-
842 dimensionalized by a^2.

843

844

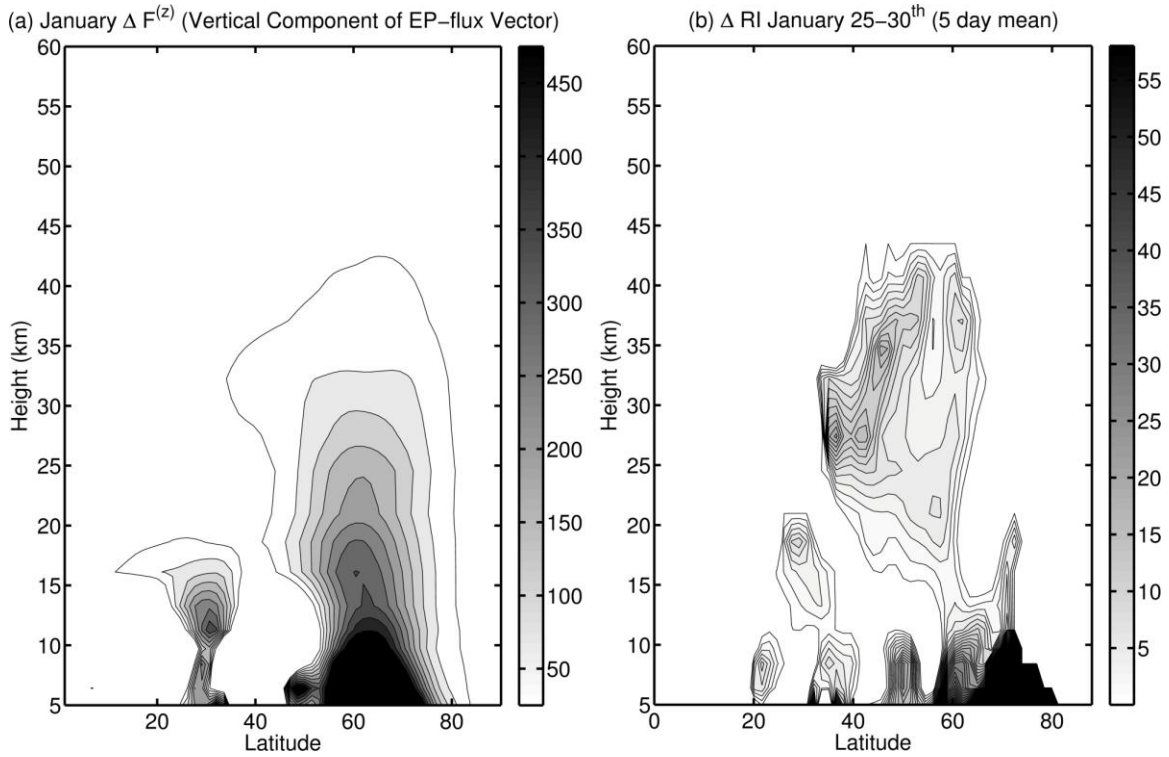

Figure 6. (a) Contours of the difference (3DO3 minus ZMO3) in ensemble mean vertical component of the EP-flux vector for January. Units are 1×10^{-9} kg•m s^{-2} and the contour interval is 5×10^{-8} kg•m s^{-2}. (b) Difference in the late January n_s^2 for the period between January 25-31. For visual clarity, the n_s^2 data was filtered so that the n_s^2 is plotted only in regions where the EP-flux divergence is less than the same minimum threshold value (~ -25×10^6 kg s^{-2}) used when plotting the EP-flux vectors in Figures 1b and 2b; see Figure 4a for EP-flux divergence scale.

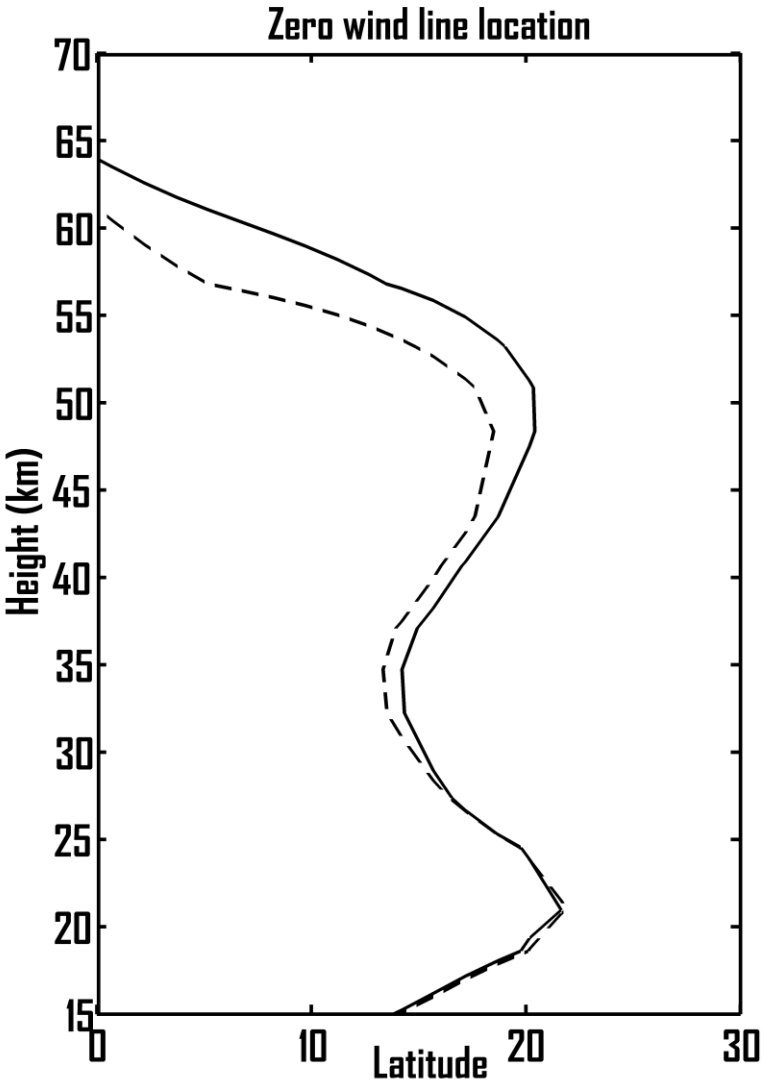

854

855 **Figure 7**. Location of February Northern Hemisphere zero wind line for 3DO3 (solid

856 line) and ZMO3 (dashed line).

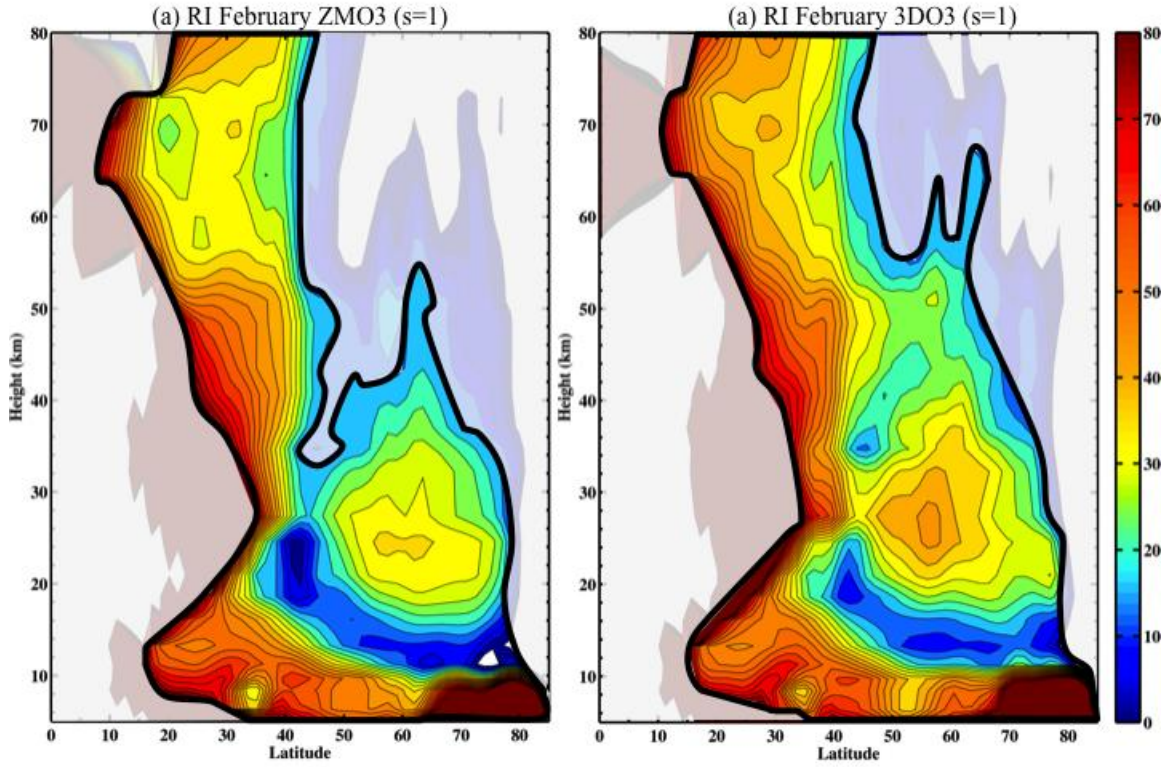

Figure 8. Monthly averaged n_s^2 for February: (a) ZMO3 for planetary wave s=1; and (b) 3DO3 for planetary wave s=1. The n_s^2 scale extends from red to blue, which corresponds with large to small n_s^2, respectively; regions where planetary waves are evanescent (n_s^2<0) are denoted by white space. We indicate the shape of the PWG by choosing a specific, though arbitrary, contour for n_s^2. Irrespective of the choice of the contour, however, the shape of the PWG remains qualitatively unchanged. The solid black line that outlines the PWG traces the 15 and 65 n_s^2 contours on the poleward and equatorward side of the PWG, respectively. In all plots, n_s^2 has been non-dimensionalized by a^2; the contour interval is 4.

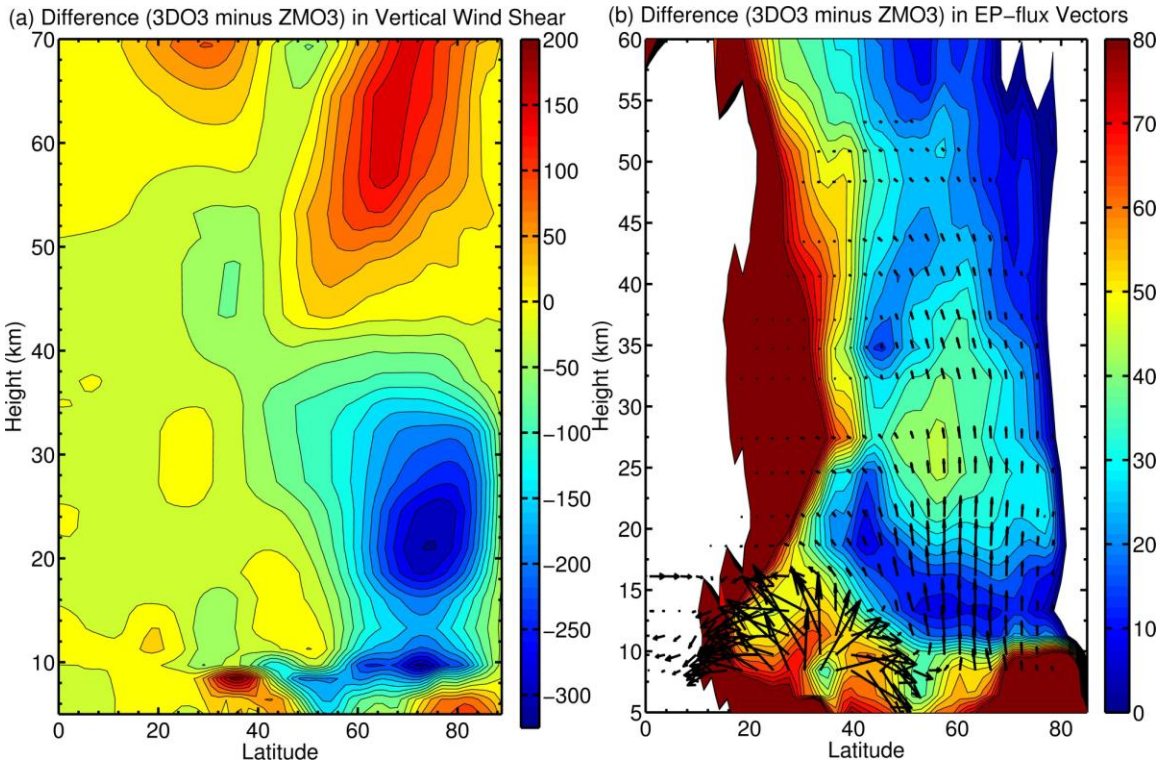

867

868 **Figure 9**. (a) The difference (3DO3 minus ZMO3) in the ensemble-mean vertical wind
869 shear for February; the contour interval is in units of m s^{-2}. (b) The difference (3DO3
870 minus ZMO3) in the EP-flux vectors for February; the ensemble mean February 3DO3
871 n_s^2 is plotted in the background for reference. As in Figures 1 and 2, the EP-flux vectors
872 in (b) were filtered so that vectors are only plotted in regions where the EP-flux
873 divergence is less than ~ -25x10^6 kg s^{-2}. The scaling of the EP-flux vectors is discussed
874 in Section 2.

875

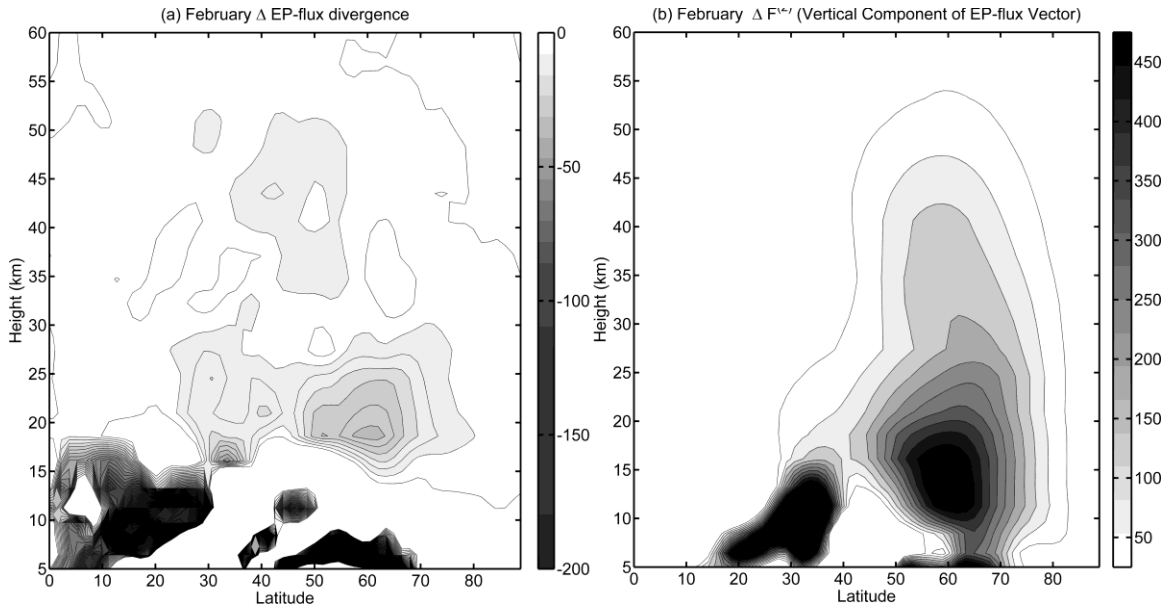

876

877 **Figure 10.** (a) February ensemble-mean difference (3DO3 minus ZMO3) in the EP-flux
878 convergence. The units are $1x10^{6}$ kg s^{-2} and the contour interval is $5x10^{6}$ kg s^{-2}. (b)
879 Contours of the difference (3DO3 minus ZMO3) in ensemble mean vertical component of
880 the EP-flux vector for February. The units are $1x10^{-9}$ kg•m s^{-2} and the contour interval is
881 $5x10^{-8}$ kg•m s^{-2}.